Non-orthogonal FDTD Methods

J. Alan Roden, Aerospace Corporation

I. Abstract

This paper presents an in-depth tutorial on the non-orthogal Finite Difference Time-domain Method (NFDTD). The mathematical formulation as well as the details of implementation are presented in detail. A variety of examples are presented along with discussion of some of the common problems associated with the method.

II. Introduction

The Finite-Difference Time-Domain technique has captured much attention since the conception of the Yee [1] cell in the 1960's. It is easily applied in an orthogonal coordinate system. Here the derivatives which are present in the curl operations of Maxwell's equations are naturally applied to the fields which lie on the underlying orthogonal grid. Unfortuneately, when curved bodies requiring high accuracy are modeled, an orthogonal implementation of the FDTD technique can lead to a forbidding computational task. While increasingly finer discretization will diminish dispersion related errors, accomplishing a true representation of the geometry features can be impractical.

To overcome this problem, it desirable that the underlying coordinate system naturally conform to the contours of the physical boundaries of the problem geometry. In the early work of Stratton [2] and later Holland [3], it was demonstrated that if a geometry may be represented by a global curvilinear coordinate system, the FDTD algorithm may be efficiently applied leading to a second order accurate solution in both time and space. This is accomplished by expressing and solving Maxwell's curl equations in the general curvilinear space. This methodology will be referred to as the globally non-orthogonal finite-difference time-domain or GNFDTD method in this work. Later, it was found that the GNFDTD technique can also be efficiently applied on a local basis [5] in those cases where a global curvilinear coordinate system was not practical. This technique is called the NFDTD technique. These methods both rely on a structured grid which is either regular or irregular in nature.

Additionally, Madsen[6], Gedney[7] and others have introduced a DSI (Discrete Surface Integral) method which supports an unstructured grid and can be much more effective in modeling arbitrarily shaped contours with a much more robust grid. This family of sulutions generally requires a complementary gridding package such as IDEAS. Other techniques have also been introduced based on local grid deformation such as the contour path (CP-FDTD[9]) and the conformal (CFDTD[10]) techniques. These techniques tend to be less general in nature.

Each of these methods conforms to curved bodies with differing complexities, differing stability criteria, and differing accuracies. The mathematical form of these techniques is described in the previous citations as well as in [8]. In this work, a detailed analysis of the NFDTD and GNFDTD methods are given and the proper implementation of the underlying constructs is illustrated. Furthermore, discussion of there applicability and shortcomings will be presented.

III. The FDTD Technique in Global Curvilinear Coordinates

In problems where the geometry conforms to a globally defined curvature, the globally non-orthogonal FDTD technique (GNFDTD) may be applied . In such cases, a set of global curvilinear coordinates $\left(\overrightarrow{u}^1,\ \overrightarrow{u}^2,\ \overrightarrow{u}^3\right)$ may be defined such that each position in the orthogonal space is given by a position vector of the form

$$\overrightarrow{r}\left(x,y,z\right)=\overrightarrow{r}\left(u^1,u^2,u^3\right). \tag{1}$$

For a given point $P\left(u^1, u^2, u^3\right)$ a set of vectors is defined by [2]

$$\overrightarrow{a}_1 = \frac{\partial \overrightarrow{r}}{\partial u^1} \qquad \overrightarrow{a}_2 = \frac{\partial \overrightarrow{r}}{\partial u^2} \qquad \overrightarrow{a}_3 = \frac{\partial \overrightarrow{r}}{\partial u^3}. \tag{2}$$

These vectors are referred to as the unitary vectors for the point P and they define the unitary axes of the general curvilinear space . These vectors are typically not of unit length. An alternate set of vectors called the contravariant vectors are denoted by superscripts and are the reciprocals of these vectors. These vectors are defined through the relation

$$\begin{aligned} \overrightarrow{a}^1 &= \frac{\overrightarrow{a}_2 \times \overrightarrow{a}_3}{\sqrt{g}} \\ \overrightarrow{a}^2 &= \frac{\overrightarrow{a}_3 \times \overrightarrow{a}_1}{\sqrt{g}} \\ \overrightarrow{a}^3 &= \frac{\overrightarrow{a}_1 \times \overrightarrow{a}_2}{\sqrt{g}} \end{aligned} \tag{3}$$

where g is the determinant of the metric tensor $[g]$ defined by

$$g_{i,j} = \overrightarrow{a}_i \cdot \overrightarrow{a}_j \tag{4}$$

or alternately

$$\sqrt{g} = \overrightarrow{a}_i \cdot \left(\overrightarrow{a}_{(i+1) \bmod 3} \times \overrightarrow{a}_{(i+2) \bmod 3}\right). \tag{5}$$

The coordinate system defined by these two sets of vectors is illustrated in Figure 1. Due to their reciprocal relation, it can be shown that

$$\overrightarrow{a}_i \cdot \overrightarrow{a}^j = \delta_{i,j} \tag{6}$$

where $\delta_{i,j}$ is the Kronecker delta function. This identity can easily be shown by using the definition of the contravariant vectors given in (3). For example

$$\overrightarrow{a}_1 \cdot \overrightarrow{a}^1 = \frac{\overrightarrow{a}_1 \cdot (\overrightarrow{a}_2 \times \overrightarrow{a}_3)}{\sqrt{g}} = 1 \tag{7}$$

$$\overrightarrow{a}_2 \cdot \overrightarrow{a}^1 = \frac{\overrightarrow{a}_2 \cdot (\overrightarrow{a}_2 \times \overrightarrow{a}_3)}{\sqrt{g}} = 0. \tag{8}$$

As was shown by Stratton, the vector fields in the orthogonal space are related to vector fields of the general curvilinear space through the relation

$$\overrightarrow{F} = \sum_{i=1}^{3} f^i \overrightarrow{a}_i \tag{9}$$

where f^i is the contravariant field vector whose vector direction is defined by the unitary vectors $\overrightarrow{a}_j, \overrightarrow{a}_k \neq \overrightarrow{a}_i$ and $\overrightarrow{F}$ represents the vector fields of an orthogonal space. Also, because contravariant and covariant vectors are a reciprocal set the reciprocal relation exists of

$$\overrightarrow{F} = \sum_{i=1}^{3} f_i \overrightarrow{a}^i. \tag{10}$$

A set of metrics may also be defined for the contravariant vectors $\overrightarrow{a}^i$ as

$$g^{i,j} = \overrightarrow{a}^i \cdot \overrightarrow{a}^j \tag{11}$$

using these metrics the vector field components in the general curvilinear space may also be related as

$$\begin{aligned} f_i &= \sum_{j=1}^{3} g_{i,j} f^j \\ f^i &= \sum_{j=1}^{3} g^{i,j} f_j. \end{aligned} \tag{12}$$

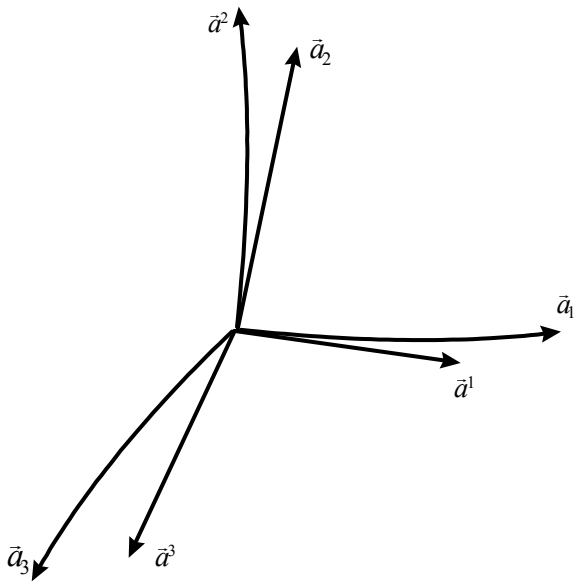

Figure 1 – Unitary and reciprocal vectors.

Using (6), (9) and (11) it can easily be shown that the covariant and contravariant field components are related to those in the orthogonal space by the relations

$$f_i = \overrightarrow{a}_i \cdot \overrightarrow{F} \tag{13}$$

and

$$f^i = \overrightarrow{a}^i \cdot \overrightarrow{F}. \tag{14}$$

The fields in the general curvilinear space are of geometry dependent units. To obtain these field values in geometry independent units the normalization of

$$\overline{F}_i = \frac{F_i}{\sqrt{g_{ii}}} \tag{15}$$

and

$$\overline{F}^i = \frac{F^i}{\sqrt{g^{ii}}} \tag{16}$$

may be applied.

Maxwell's curl equations may be constructed using the concepts outlined above. To this end, the formulation of the $\widehat{a}^1$ component of the curl operation is examined in the general curvilinear space. The right hand side of this component may be approximated as

$$\nabla \times \overrightarrow{F} \cdot \widehat{a}^1 = \lim_{C \to 0} \frac{1}{A} \oint_C \overrightarrow{F} \cdot d\overrightarrow{l} \tag{17}$$

where A is the area of the surface bounded by the covariant vectors u_2 and u_3 as illustrated in Figure 2. The discretized line integral around the contour C is given in terms of the covariant field values as

$$\oint \overrightarrow{F} \cdot d\overrightarrow{l} = \left\{ \left(F_3 du^3\right)_{u^2+du^2} - \left(F_3 du^3\right)_{u^2} - \left(F_2 du^2\right)_{u^3+du^3} + \left(F_2 du^2\right)_{u^3} \right\} \tag{18}$$

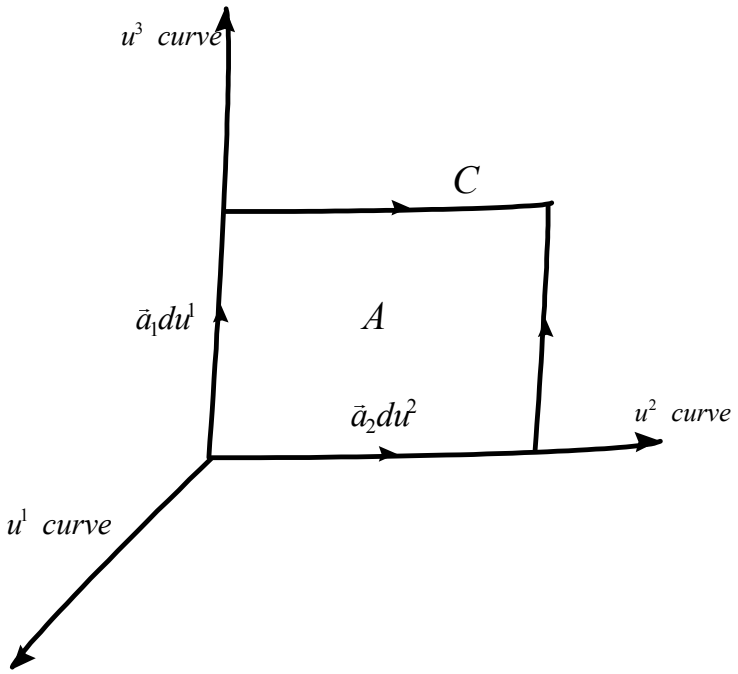

Figure 2 – Illustration of the curl operation in general curvilinear coordinates.

and approximating these differences by the first terms of the Taylor series expansion we may write

$$\oint \overrightarrow{F} \cdot d\overrightarrow{l} = \left\{ \frac{\partial F_3}{\partial u^2} - \frac{\partial F_2}{\partial u^3} \right\} du^2 du^3. \tag{19}$$

The area of the surface bounded by C is given by

$$\begin{aligned} A &= \sqrt{\overrightarrow{a}_2 \times \overrightarrow{a}_3 \cdot \overrightarrow{a}_2 \times \overrightarrow{a}_3} du^2 du^3 \\ &= \left| \overrightarrow{a}^1 \right| \sqrt{g} du^2 du^3 \end{aligned} \tag{20}$$

and the unit normal in the direction of $\overrightarrow{a}^1$ is given by

$$\frac{\overrightarrow{a}^1}{\sqrt{\overrightarrow{a}^1 \cdot \overrightarrow{a}^1}} \tag{21}$$

so

$$\nabla \times \overrightarrow{F} \cdot \widehat{a}^1 = \frac{1}{\sqrt{g}} \left\{ \frac{\partial F_3}{\partial u^2} - \frac{\partial F_2}{\partial u^3} \right\}. \tag{22}$$

The discretization of the other components of the curl operation in a similar way, leads to Maxwell's equations for a sourceless media in the general curvilinear space which are

$$j\omega\mu H^1 = -\frac{1}{\sqrt{g}} \left\{ \frac{\partial E_3}{\partial u^2} - \frac{\partial E_2}{\partial u^3} \right\} \tag{23}$$

$$j\omega\mu H^2 = -\frac{1}{\sqrt{g}} \left\{ \frac{\partial E_1}{\partial u^3} - \frac{\partial E_3}{\partial u^1} \right\} \tag{24}$$

$$j\omega\mu H^3 = -\frac{1}{\sqrt{g}} \left\{ \frac{\partial E_2}{\partial u^1} - \frac{\partial E_1}{\partial u^2} \right\} \tag{25}$$

$$j\omega\epsilon_0\epsilon_r E^1 + \sigma E^1 = \frac{1}{\sqrt{g}}\left\{\frac{\partial H_3}{\partial u^2} - \frac{\partial H_2}{\partial u^3}\right\} \tag{26}$$

$$j\omega\epsilon_0\epsilon_r E^2 + \sigma E^2 = \frac{1}{\sqrt{g}}\left\{\frac{\partial H_1}{\partial u^3} - \frac{\partial H_3}{\partial u^1}\right\} \tag{27}$$

$$j\omega\epsilon_0\epsilon_r E^3 + \sigma E^3 = \frac{1}{\sqrt{g}}\left\{\frac{\partial H_2}{\partial u^1} - \frac{\partial H_1}{\partial u^2}\right\}. \tag{28}$$

A. Efficient Implementation

The efficient implementation of (23) through (28) in the general curvilinear space is now illustrated. It is noted that these equations have a form which images the standard orthogonal FDTD technique. Therefore, the discretization of these equations is accomplished in a similar way. Specifically, a central difference approximation is applied both in space and time to the differential operators embodied in (23) through (28). To enhance the computational efficiency of this method the following substitutions are made

$$\begin{aligned} \overrightarrow{h_i} &= H_i\sqrt{\eta_0}\Delta_i \\ \overrightarrow{e_i} &= \frac{E_i}{\sqrt{\eta_0}}\Delta_i \end{aligned} \tag{29}$$

so that the update equations are now written as

$$e^{1^{n+1}}_{i,j,k} = a^e_{i,j,k}e^{1^n}_{i,j,k} + b^{e1}_{i,j,k}\left(h^{n+\frac{1}{2}}_{3_{i,j,k}} - h^{n+\frac{1}{2}}_{3_{i,j-1,k}} - h^{n+\frac{1}{2}}_{2_{i,j,k}} + h^{n+\frac{1}{2}}_{2_{i,j,k-1}}\right) \tag{30}$$

$$e^{2^{n+1}}_{i,j,k} = a^e_{i,j,k}e^{2^n}_{m,n,p} + b^{e_2}_{i,j,k}\left(h^{n+\frac{1}{2}}_{1i,j,k} - h^{n+\frac{1}{2}}_{1_{i,j,k-1}} - h^{n+\frac{1}{2}}_{3_{i,j,k}} + h^{n+\frac{1}{2}}_{3_{i-1,j,k}}\right) \tag{31}$$

$$e^{3^{n+1}}_{i,j,k} = a^e_{i,j,k}e^{3^n}_{i,j,k} + b^{e_3}_{i,j,k}\left(h^{n+\frac{1}{2}}_{2i,j,k} - h^{n+\frac{1}{2}}_{2_{i-1,j,k}} - h^{n+\frac{1}{2}}_{1_{i,j,k}} + h^{n+\frac{1}{2}}_{1_{i,j-1,k}}\right) \tag{32}$$

$$h^{1^{n+\frac{1}{2}}}_{i,j,k} = h^{1^{n-\frac{1}{2}}}_{i,j,k} - b^{h1}_{i,j,k}\left(e^n_{3_{i,j+1,k}} - e^n_{3_{i,j,k}} - e^n_{2i,j,k+1} + e^n_{2_{i,j,k}}\right) \tag{33}$$

$$h^{2^{n+\frac{1}{2}}}_{i,j,k} = h^{2^{n-\frac{1}{2}}}_{i,j,k} - b^{h_2}_{i,j,k}\left(e^n_{1_{i,j,k+1}} - e^n_{1_{i,j,k}} - e^n_{3i+1,j,k} + e^n_{3_{i,j,k}}\right) \tag{34}$$

$$h^{3^{n+\frac{1}{2}}}_{i,j,k} = h^{3^{n-\frac{1}{2}}}_{i,j,k} - b^{h_3}_{i,j,k}\left(e^n_{2_{i+1,j,k}} - e^n_{2_{i,j,k}} - e^n_{1_{i,j+1,k}} + e^n_{1_{i,j,k}}\right) \tag{35}$$

where

$$a^e_{i,j,k} = \frac{2 - c_0\Delta_t\sigma\eta_0}{2 + \sigma\eta_0 c_0\Delta_t} \tag{36}$$

$$b^{e1}_{i,j,k} = \frac{2c_0\Delta_t\Delta_{u^1}}{(2+\sigma\eta_0 c_0\Delta_t)\,\epsilon_{r_{i,j,k}}\sqrt{g}\Delta_{u^2}\Delta_{u^3}}\ , \quad b^{e2}_{i,j,k} = \frac{2c_0\Delta_t\Delta_{u^2}}{(2+\sigma\eta_0 c_0\Delta_t)\,\epsilon_{r_{i,j,k}}\sqrt{g}\Delta_{u^1}\Delta_{u^3}} \tag{37}$$

$$b^{e3}_{i,j,k} = \frac{2c_0\Delta_t\Delta_{u^3}}{(2+\sigma\eta_0 c_0\Delta_t)\,\epsilon_{r_{i,j,k}}\sqrt{g}\Delta_{u^1}\Delta_{u^2}} \tag{38}$$

$$b^{h1}_{i,j,k} = \frac{c_0\Delta_t\Delta_{u^1}}{\sqrt{g}\Delta_{u^2}\Delta_{u^3}}, \qquad b^{h2}_{i,j,k} = \frac{c_0\Delta_t\Delta_{u^2}}{\sqrt{g}\Delta_{u^1}\Delta_{u^3}}, \qquad b^{h3}_{i,j,k} = \frac{c_0\Delta_t\Delta_{u^3}}{\sqrt{g}\Delta_{u^1}\Delta_{u^2}}. \tag{39}$$

Each of these coefficients may be precomputed to enhance the computational efficiency of the updates.

The update expressions of (30) through (35) are updated explicitly based on prior computed covariant field values. Since only contravariant fields are known explicitly from the update equations, a set of auxiliary expressions must be introduced which relates the covariant fields to the contravariant fields computed by (30) through (35). This is accomplished through the relation expressed in (12). Equation (12) requires that all three field components be known at the same position in space. However, due to the staggered nature of the grid the computed fields are not collocated. Therefore, to achieve spatial alignment the fields values which share the endpoints of desired covariant field value f_i are averaged to give a second order accurate approximation of the covariant fields. The resultant projections are given by

$$E_{1_{i,j,k}} = g_{11}E^1_{i,j,k} + \frac{g_{12}}{4}\left(E^2_{i,j,k} + E^2_{i+1,j,k} + E^2_{i,j-1,k} + E^2_{i+1,j-1,k}\right) + \frac{g_{13}}{4}\left(E^3_{i,j,k} + E^3_{i+1,j,k} + E^3_{i,j,k-1} + E^3_{i+1,j,k-1}\right) \tag{40}$$

$$E_{2_{i,j,k}} = g_{22}E^2_{i,j,k} + \frac{g_{21}}{4}\left(E^1_{i,j,k} + E^1_{i,j+1,k} + E^1_{i-1,j,k} + E^1_{i-1,j+1,k}\right) + \frac{g_{23}}{4}\left(E^3_{i,j,k} + E^3_{i,j+1,k} + E^3_{i,j,k-1} + E^3_{i,j+1,k-1}\right) \tag{41}$$

$$E_{3_{i,j,k}} = g_{33}E^3_{i,j,k} + \frac{g_{31}}{4}\left(E^1_{i,j,k} + E^1_{i-1,j,k} + E^1_{i,j,k+1} + E^1_{i-1,j,k+1}\right) + \frac{g_{32}}{4}\left(E^2_{i,j,k} + E^2_{i,j-1,k} + E^2_{i,j,k+1} + E^2_{i,j-1,k+1}\right) \tag{42}$$

for the electric field and for the magnetic field

$$H_{1_{i,j,k}} = g_{11}H^1_{i,j,k} + \frac{g_{12}}{4}\left(H^2_{i,j,k} + H^2_{i-1,j,k} + H^2_{i,j+1,k} + H^2_{i-1,j+1,k}\right) + \frac{g_{13}}{4}\left(H^3_{i,j,k} + H^3_{i-1,j,k} + H^3_{i,j,k+1} + H^3_{i-1,j,k+1}\right) \tag{43}$$

$$H_{2_{i,j,k}} = g_{22}H^2_{i,j,k} + \frac{g_{21}}{4}\left(H^1_{i,j,k} + H^1_{i,j-1,k} + H^1_{i+1,j,k} + H^1_{i+1,j-1,k}\right) + \frac{g_{23}}{4}\left(H^3_{i,j,k} + H^3_{i,j-1,k} + H^3_{i,j,k+1} + H^3_{i,j-1,k+1}\right) \tag{44}$$

$$H_{3_{i,j,k}} = g_{33}H^3_{i,j,k} + \frac{g_{31}}{4}\left(H^1_{i,j,k} + H^1_{i+1,j,k} + H^1_{i,j,p-1} + H^1_{i+1,j,p-1}\right) + \frac{g_{32}}{4}\left(H^2_{i,j,k} + H^2_{i,j+1,k} + H^2_{i,j,k-1} + H^2_{i,j+1,k-1}\right). \tag{45}$$

The stability relation for non-orthogonal grids takes a similar form to that for orthogonal grids[5]. It is derived by assuming a plane wave propagation of the form

$$\overrightarrow{E}\left(u^1, u^2, u^3, t\right) = \overrightarrow{E}_0 e^{-j\left(k_1 u^1 + k_2 u^2 + k_3 u^3\right)} \tag{46}$$

in the general curvilinear space where

$$k_i = \widehat{a}_i \cdot \overrightarrow{k}. \tag{47}$$

Subsequently, the wave equation is formulated in the curvilinear space and the growth factor constrained as

$$|\alpha| = \left|\frac{\overrightarrow{E}^{n+1}}{\overrightarrow{E}^{n}}\right| \leq 1.0. \tag{48}$$

This leads to a stability relation of

$$\Delta_t \leq \frac{1}{c\sqrt{\sum_{j=1}^{3}\sum_{i=1}^{3}\frac{|g^{i,j}|}{\Delta_{u^i}\Delta_{u^j}}}} \tag{49}$$

for the FDTD in globally curvilinear coordinates. A complete proof is found in [8], [5].

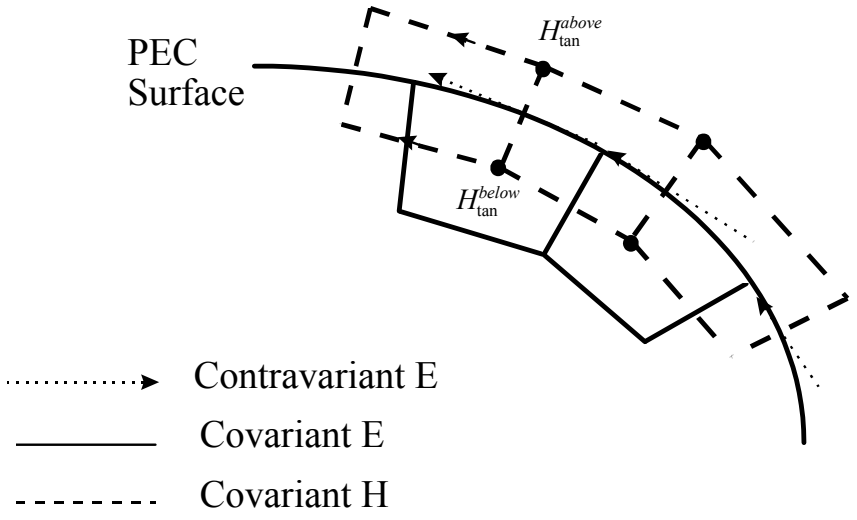

Figure 3 – Orientation of contravariant and covariant E field vectors on a perfectly conducting surface.

B. Boundary Conditions

Physical boundary conditions are present in any problem geometry and are essential for grid termination. These physical boundary conditions include the perfect electric conductor (PEC) and the perfect magnetic conductor (PMC). While these bondaries are easily implemented in an orthogonal space, a bit more consideration is required in the non-orthogonal space. This is due to the fact there are two sets of fields at each boundary which must be terminated: the contravariant and covariant fields. Consider the case of the PEC boundary condition for a curved metal surface in the general curvilinear space. This is illustrated in Figure 3. It is clear from this illustration that the covariant $\overrightarrow{E}$ fields which are tangential at the surface must be set to zero as in the orthogonal FDTD case. There is no basis for setting the contravariant fields to zero at the surface, however. In order to update the contravariant electric fields along the surface of the conductor, the covariant magnetic fields which surround the field location must be known. The proper implementation of the PEC boundary condition requires that these fields be defined such that in the limit as the grid becomes orthogonal, the boundary conditions of the conductor are satisfied. A proper update strategy for these fields is accomplished through imaging of the tangential covariant magnetic fields from just above the conductor surface as

$$H_{\tan_{below}} = H_{\tan_{above}}.$$

The contravariant magnetic field values interior to the conductor are explicitly set to zero. As a result, the only contributing term to the line integral in the update for the contravariant electric field at the surface comes from the covariant magnetic field which passes through the surface of the conductor, which should be the case.

The PMC boundary condition is implemented in an analogous manner to the orthogonal case. For consistency, both the contravariant and covariant field components are imaged.

C. GNFDTD Results

A non-orthogonal general curvilinear space is applicable to a limited set of problems. Two examples of such a space are given by a globally skewed grid and a globally twisted grid. While the globally skewed grid is not of great value, it does serve to demonstrate some of the qualities of a globally nonorthogonal implementation

A globally skewed grid might find application in some waveguide systems. As an illustration of the application of the FDTD technique in a globally skewed grid, a microstrip planar microstrip transmission

line is analyzed. The transmission line consists of conductor of width 2.413 mm placed at a height of 0.795 mm above a perfectly conducting ground plane. The two conductors are separated by a dielectric substrate with a relative permittivity of $\epsilon_r = 2.2$. In order to compare the merits of the orthogonal FDTD and the GNFDTD methods, the problem is analyzed in three different manners: Using orthogonal grids and with the conductor aligned along the x axis, using a globally nonorthogonal grid (GNFDTD) where the y axis is skewed at 45 degrees with respect to the x axis, and using an orthogonal grid with a 45 degree skewed microstrip where stairstepping is used. The formulation of the GNFDTD coordinate system is presented in the following section followed by the three results. For the orthogonal grid analysis a discretization of $\Delta_x = \Delta_y = 0.3447\ mm$, $\Delta_z = 0.265\ mm$ was used. The grid is terminated using a uniaxial PML implementation which is documented in [15].

The position vector for a global curvilinear coordinate system which naturally conforms to this geometry is given by

$$\overrightarrow{r}\left(u^1, u^2, u^3\right) = \widehat{x}u^1 + \widehat{y}\left(u^2 + u^1 \tan\theta\right) + \widehat{z}u^3 \tag{50}$$

from which the unitary vectors are given as

$$\begin{aligned} \overrightarrow{a}_1 &= \widehat{x} + \widehat{y}\tan\theta \\ \overrightarrow{a}_2 &= \widehat{y} \\ \overrightarrow{a}_3 &= \widehat{z} \end{aligned} \tag{51}$$

where θ is the angle of the skew with respect to the x axis. The g matrix for this grid is independent of position and is given by

$$g_{i,j} = \begin{bmatrix} 1+\tan^2\theta & \tan\theta & 0 \\ \tan\theta & 1 & 0 \\ 0 & 0 & 1 \end{bmatrix} \tag{52}$$

and $\sqrt{g} = 1.0$.

The orientation of the skewed microstrip line in the GNFDTD grid which corresponds to (3) is illustrated in Figure 4 while the orthogonal grid which uses stairstepping approximation of the geometry is illustrated in Figure 5.

The bend in the orthogonal grid model is due to the absorbing boundary. For a conductor terminating normally into the PML absorbing boundary the energy is absorbed optimally and negligible reflection error is produced. The termination is much less than ideal for an arbitrary angular termination. For this reason, the microstrip is turned 5 cells before the absorbing boundary such that it enters the boundary orthogonally. A second cost associated with the orthogonal implementation of this geometry occurs because the problem does not naturally align with the rectangular coordinate axes. As a result, the width of the numerical space must be increased linearly as the length of the line increases. This leads to greater computational costs.

In contrast to the orthogonal FDTD grid of Figure 5, the GNFDTD modeled microstrip terminates directly into the end wall boundary. This leads to an excellent impedance match across the frequency band studied. Also, the microstrip line is aligned naturally to the grid so that increasing line length does not increase the transverse dimensions of the problem. The proper design of the absorbing boundary in non-orthogonal coordinates is discussed further in Chapter 4.

The results of the skewed microstrip analysis are demonstrated in Figure 6 for the GNFDTD method and the orthogonal FDTD method. The two results are compared to the non-skewed line to demonstrate the error introduced by the skew. It is observed that at lower frequencies the orthogonal staircasing approximation is slightly more accurate than the GNFDTD. At higher frequencies, however, the dispersion is considerably higher for the orthogonal FDTD solution leading to significant error. This can be attributed to both increased sensitivity to the discontinuities caused by staircasing and the bend which is implemented to achieve better absorbing boundary performance. It should be noted that much worse performance was observed when the microstrip line did not enter the absorbing boundary orthogonally. The computation grid of the orthogonal FDTD was $70 \times 110 \times 20$ while that of the GNFDTD was $70 \times 47 \times 20$. The GNFDTD implementation required roughly twice the computation time of the orthogonal FDTD implementation. It should be noted, however, that the accuracy of the physical representation of the geometry is highly dependent on both the transverse and longitudinal discretization for the orthogonal model of the 45 degree

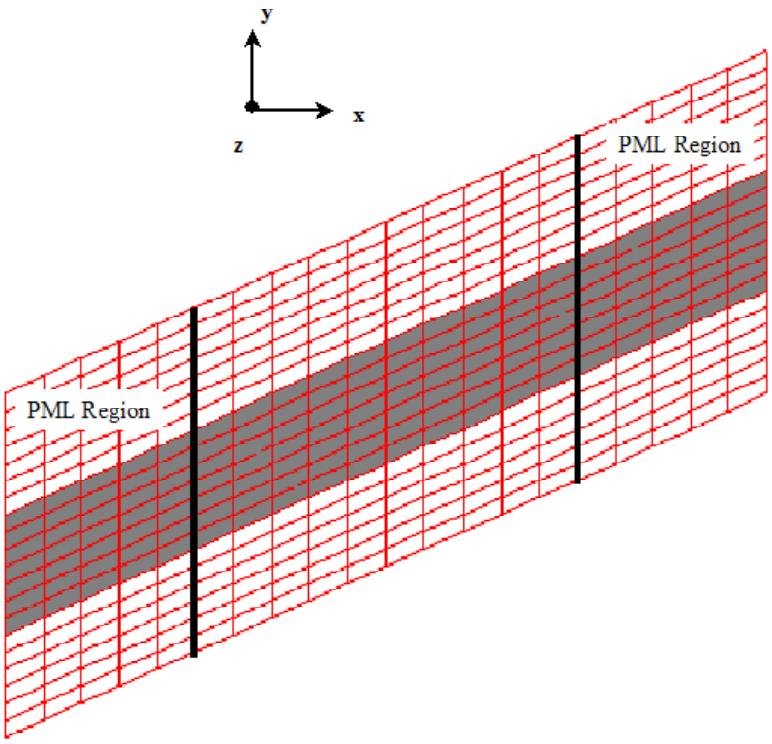

Figure 4 – Overhead view (-Z viewing direction) of a 45 degree skewed microstrip as represented by a globally nonorthogonal skewed grid.

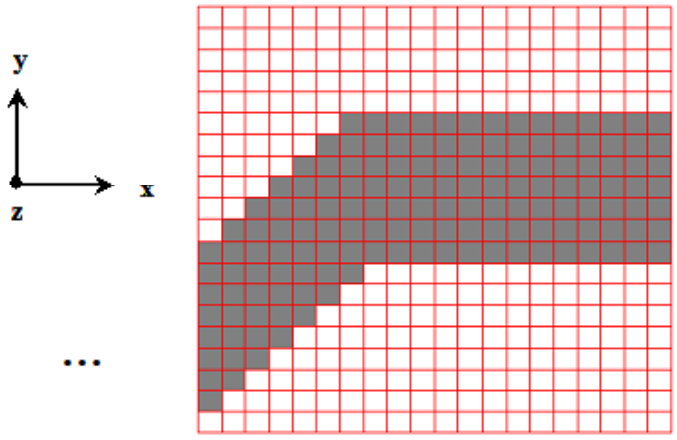

Figure 5 – Illustration of termination region discretization of skewed microstrip transmission line on an orthogonal grid.

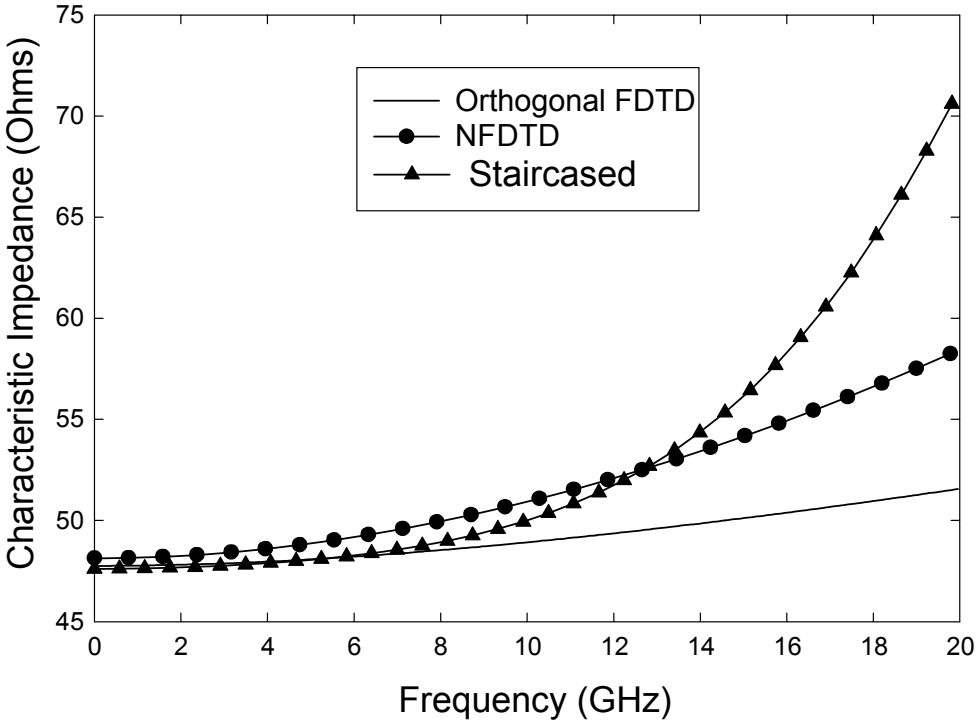

Figure 6 – Analysis of microstrip transmission line with 45 degree skew using orthogonal and non-orthogonal FDTD.

line. For the nonorthogonal implementation, the longitudinal discretization is only driven by the desired frequency range of the simulation, thus a much coarser grid can likely be used.

As a second illustration of the application of a globally non-orthogonal grid in a general curvilinear coordinate system, a twisted pair round wire transmission line is analyzed. The geometry consists of two round wires, whose cross-section is approximated by staircasing here, with a twist applied such that the waveguide undergoes a rotation of approximately 360 degrees over the length of the transmission line. Some clear advantages may be gained by using the proper coordinate system for analyzing complex geometries such as a waveguide or an antenna which have a helical twist. Certainly, accuracy is enhanced by properly conforming to the geometry. Equally important, greater solution efficiency may be achieved by taking advantages of the problem symmetries which are present in the conformal space. Such is the case for a pair of round wires which are twisted along the longitudinal direction (twisted pair line). The application of a twisted global curvilinear coordinate system as described in the following paragraphs allows the modeling of the twisted geometry using the same odd/even symmetric boundaries as were used for the straight wire case. Specifically, PMC and PEC planes are implemented to effectively reduce the problem size to twenty-five percent of the original geometry.

In a twisted coordinate system defined by

$$\overrightarrow{r}\left(u^1,u^2,u^3\right)=\widehat{x}\left(u^1\cos\theta-u^2\sin\theta\right)+\widehat{y}\left(u^1\sin\theta+u^2\cos\theta\right)+\widehat{z}u^3 \tag{53}$$

where $\theta = pz$ and p is the pitch density of the line, the u^1, u^2 coordinate axes rotate by an angle θ as the u^3dimension is increased. The unitary vectors for this space are given by

$$\begin{aligned}
\overrightarrow{a}_1 &= \widehat{x}\cos\theta+\widehat{y}\sin\theta \\
\overrightarrow{a}_2 &= -\widehat{x}\sin\theta+\widehat{y}\cos\theta \\
\overrightarrow{a}_3 &= -\widehat{x}p\left(u^1\sin\theta+u^2\cos\theta\right)+\widehat{y}p\left(u^1\cos\theta-u^2\sin\theta\right)+\widehat{z}
\end{aligned}$$

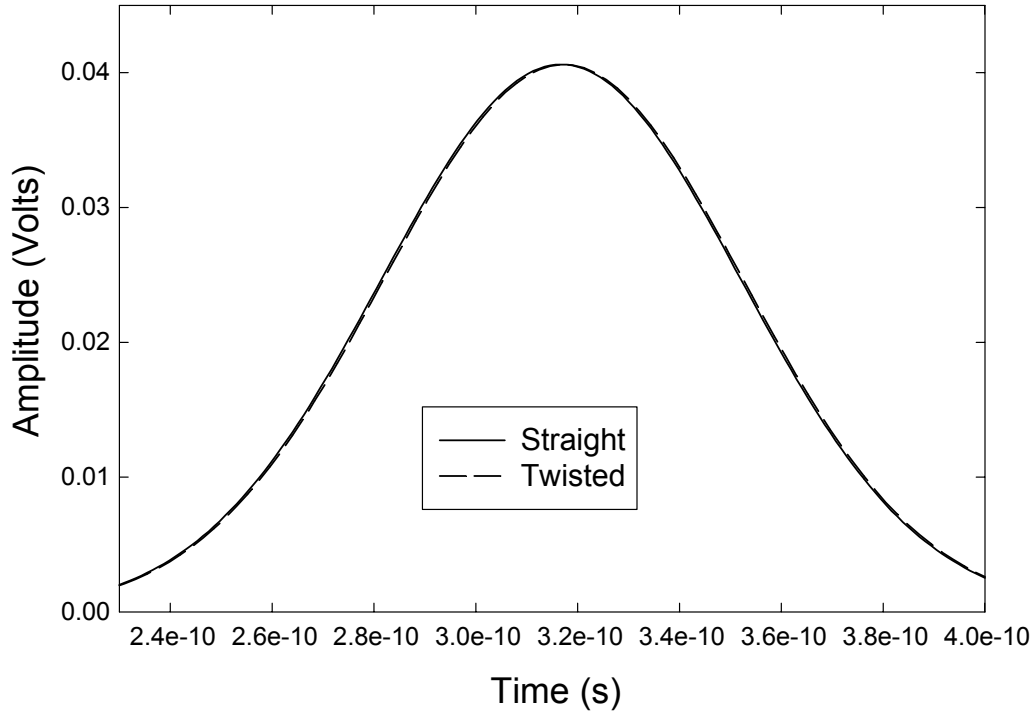

Figure 7 – Time-Domain results of twisted and untwisted transmission line excited by a Gaussian source.

and the metric coefficient matrix is

$$g_{i,j}\left(u^1,u^2\right)=\begin{bmatrix}1 & 0 & -u^2p\\ 0 & 1 & u^1p\\ -u^1p & u^1p & 1+p^2\left(u^{1^2}+u^{2^2}\right)\end{bmatrix} \tag{54}$$

where $\theta = pz$ and p is the pitch density in radians/meter, also $\sqrt{g}=1.0$.

Presently, no analytic expression exists for the impedance of the twisted-pair transmission line studied here. One expects that if the twist is gradual a quasi-TEM mode will be supported and the field pattern will be close to that of the parallel line. Figure 7 compares the time-domain waveform which results from launching a gaussian pulse along the twisted line with $p = 315.0\ r/m$. This twist rate is typical of a twisted pair transmission line. The voltage between the two conductors is measured at two points separated by fifty cells. The time-domain results are compared to same geometry but with zero pitch.

These results show that a slight time delay is introduced for the twisted case due to the additional length traversed by the signal as a result of the twist. The length scale factor is given by $l_3 = \sqrt{g_{33}}$ and concurs with the time delay displayed.

IV. The FDTD Technique in Local Curvilinear Coordinates (NFDTD)

In the previous sections it was demonstrated that for regular geometries where the position vector for a point $P\left(u^1,u^2,u^3\right)$ could be analytically defined that general curvilinear coordinate system concepts may be employed and consequently the FDTD method is easily implemented. For many practical problems such as the round wire geometry, such a global coordinate system is not applicable. In cases such as this, general curvilinear coordinate system concepts may be introduced on a local basis [5], [3].

To this end, a structured grid is first designed to conform to the problem geometry, typically using a CAD package or similar. This grid may be chosen to align with either the electric field or magnetic field components depending on where the boundary conditions of the physical geometry are to be enforced. For

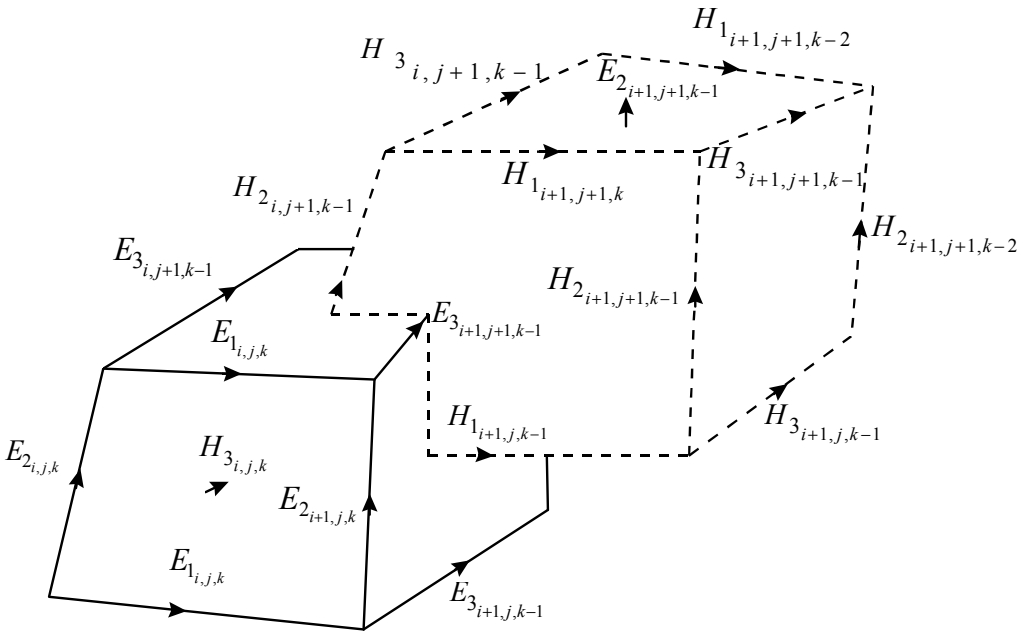

Figure 8 – Primary/Dual grid configuration for irregular grids.

this work, a primary grid is generated using a computer code such that the grid conforms to boundaries where the electrical properties may be described. A secondary grid is then generated by connecting the barycenters of the primary grid for cells which share a common face. Such a grid is illustrated in Figure 8. For a geometry which is described by an irregular grid such as Figure 8 the covariant vectors are directly defined by the grid edges of the secondary and primary grid, for example

$$\overrightarrow{A}_1 = \widehat{x}\left(u_a^1 - u_b^1\right) + \widehat{y}\left(u_a^2 - u_b^2\right) + \widehat{z}\left(u_a^3 - u_b^3\right) \tag{55}$$

where the two points a and b are the endpoints of the edge which defines $\overrightarrow{A}_1$. Each covariant vector is therefore scaled by edge length and is a linear line segment. These covariant vectors constitute the unitary vectors of the general curvilinear coordinate system. Both the NFDTD and the GNFDTD method are based on curvilinear coordinate concepts. Therefore, the identities given in (3) through (16) are still applicable. The two methods differ in manner in which the curvilinear coordinate system constructs are defined. Specifically, in the NFDTD method, the vectors about each cell face define a unique local curvilinear coordinate system. The formulation of the NFDTD method is demonstrated in the following sections.

In an irregular non-orthogonal space, Maxwell's equations are most naturally applied in their integral form. To this end, the integral form of Maxwell's equations are applied at each cell face of both the secondary and primary grid. The integral form of Maxwell's equations are given by

$$\int\int \frac{\partial \mu \overrightarrow{H}}{\partial t} \cdot d\widehat{s} = -\oint_C \overrightarrow{E} \cdot \overrightarrow{dl} \tag{56}$$

$$\int\int \left(\frac{\partial \epsilon \overrightarrow{E}}{\partial t} + \sigma \overrightarrow{E}\right) \cdot d\widehat{s} = \oint_C \overrightarrow{H} \cdot \overrightarrow{dl} \tag{57}$$

The field components of the line integral on the right hand side are naturally written in terms of the covariant fields of the general curvilinear space since these field components flow around each cell face and are scaled by the length of their respective edges. The contravariant field values have a vector direction which is normal to each cell face and therefore are the natural choice for the left hand sides of (56) and (57). Each

curvilinear component of these equations is extracted by taking the dot product of each side with the unit vector $\widehat{A^i}$. In the discretized general curvilinear space the surface integral on the left hand side of (57) is then approximated for each face as

$$\begin{aligned} \int\int \frac{\partial \mu \overrightarrow{F}}{\partial t} \cdot d\widehat{s_i} &= \frac{\partial \mu F^i}{\partial t \left| \overrightarrow{A}^i \right|} ds_i \\ &= \frac{\partial \mu F^i}{\partial t} V \end{aligned} \tag{58}$$

where V is the volume of the local coordinate system and is given by

$$V = \overrightarrow{A}_i \cdot \left(\overrightarrow{A}_{(i+1) \bmod 3} \times \overrightarrow{A}_{(i+2) \bmod 3} \right).$$

The six update equations for both the electric and magnetic field may now be written directly in the discrete space as

$$E^{1^{n+1}}_{i,j,k} = a^e_{i,j,k} E^{1^n}_{i,j,k} + b^{e1}_{i,j,k} \left(H^{n+\frac{1}{2}}_{3_{i,j,k}} - H^{n+\frac{1}{2}}_{3_{i,j-1,k}} - H^{n+\frac{1}{2}}_{2_{i,j,k}} + H^{n+\frac{1}{2}}_{2_{i,j,k-1}} \right) \tag{59}$$

$$E^{2^{n+1}}_{i,j,k} = a^e_{i,j,k} E^{2^n}_{m,n,p} + b^{e_2}_{i,j,k} \left(H^{n+\frac{1}{2}}_{1i,j,k} - H^{n+\frac{1}{2}}_{1_{i,j,k-1}} - H^{n+\frac{1}{2}}_{3_{i,j,k}} + H^{n+\frac{1}{2}}_{3_{i-1,j,k}} \right) \tag{60}$$

$$E^{3^{n+1}}_{i,j,k} = a^e_{i,j,k} E^{3^n}_{i,j,k} + b^{e_3}_{i,j,k} \left(H^{n+\frac{1}{2}}_{2i,j,k} - H^{n+\frac{1}{2}}_{2_{i-1,j,k}} - H^{n+\frac{1}{2}}_{1_{i,j,k}} + H^{n+\frac{1}{2}}_{1_{i,j-1,k}} \right) \tag{61}$$

$$H^{1^{n+\frac{1}{2}}}_{i,j,k} = H^{1^{n-\frac{1}{2}}}_{i,j,k} - b^{h1}_{i,j,k} \left(E^n_{3_{i,j+1,k}} - E^n_{3_{m,n,p}} - E^n_{2i,j,k+1} + E^n_{2_{i,j,k}} \right) \tag{62}$$

$$H^{2^{n+\frac{1}{2}}}_{i,j,k} = H^{2^{n-\frac{1}{2}}}_{i,j,k} - b^{h_2}_{i,j,k} \left(E^n_{1_{i,j,k+1}} - E^n_{1_{m,n,p}} - E^n_{3_{i+1,j,k}} + E^n_{3_{i,j,k}} \right) \tag{63}$$

$$H^{3^{n+\frac{1}{2}}}_{i,j,k} = H^{3^{n-\frac{1}{2}}}_{i,j,k} - b^{h_3}_{i,j,k} \left(E^n_{2_{i+1,j,k}} - E^n_{2_{i,j,k}} - E^n_{1_{i,j+1,k}} + E^n_{1_{i,j,k}} \right) \tag{64}$$

where

$$a^e_{i,j,k} = \frac{2 - \Delta_t \sigma}{2 + \sigma \Delta_t} \tag{65}$$

$$b^{e1}_{i,j,k} = \frac{2\Delta_t}{(2 + \sigma\Delta_t)\, \epsilon_0 \epsilon_{r_{i,j,k}} V^1_{i,j,k_e}}, \quad b^{e2}_{i,j,k} = \frac{2\Delta_t}{(2 + \sigma\Delta_t)\, \epsilon_0 \epsilon_{r_{i,j,k}} V^2_{i,j,k_e}} \tag{66}$$

$$b^{e3}_{i,j,k} = \frac{2\Delta_t \Delta_{u^3}}{(2 + \sigma\Delta_t)\, \epsilon_0 \epsilon_{r_{i,j,k}} V^3_{i,j,k_e}} \tag{67}$$

$$b^{h1}_{i,j,k} = \frac{\Delta_t}{\mu_0 V^1_{i,j,k_h}}, \qquad b^{h2}_{i,j,k} = \frac{\Delta_t}{\mu_0 V^2_{i,j,k_h}}, \qquad b^{h3}_{i,j,k} = \frac{\Delta_t}{\mu_0 V^3_{i,j,k_h}} \tag{68}$$

and

$$V^1_{i,j,k_e} = \frac{\overrightarrow{A}^e_{1_{i,j,k}} \cdot \left(\left(\overrightarrow{A}^h_{2_{i,j,k}} + \overrightarrow{A}^h_{2_{i,j,k-1}} \right) \times \left(\overrightarrow{A}^h_{3_{i,j,k}} + \overrightarrow{A}^h_{3_{i,j-1,k}} \right) \right)}{4} \tag{69}$$

$$V^1_{i,j,k_h} = \frac{\overrightarrow{A}^h_{1_{i,j,k}} \cdot \left(\left(\overrightarrow{A}^e_{2_{i,j,k}} + \overrightarrow{A}^e_{2_{i,j,k+1}} \right) \times \left(\overrightarrow{A}^e_{3_{i,j,k}} + \overrightarrow{A}^e_{3_{i,j+1,k}} \right) \right)}{4}$$

$$V^2_{i,j,k_e} = \frac{\overrightarrow{A}^e_{2_{i,j,k}} \cdot \left(\left(\overrightarrow{A}^h_{3_{i,j,k}} + \overrightarrow{A}^h_{3_{i-1,j,k}} \right) \times \left(\overrightarrow{A}^h_{1_{i,j,k}} + \overrightarrow{A}^h_{1_{i,j,k-1}} \right) \right)}{4} \tag{70}$$

$$V^2_{i,j,k_h} = \frac{\overrightarrow{A}^h_{2_{i,j,k}} \cdot \left(\left(\overrightarrow{A}^e_{3_{i,j,k}} + \overrightarrow{A}^e_{3_{i+1,j,k}} \right) \times \left(\overrightarrow{A}^e_{1_{i,j,k}} + \overrightarrow{A}^e_{1_{i,j,k+1}} \right) \right)}{4} \tag{71}$$

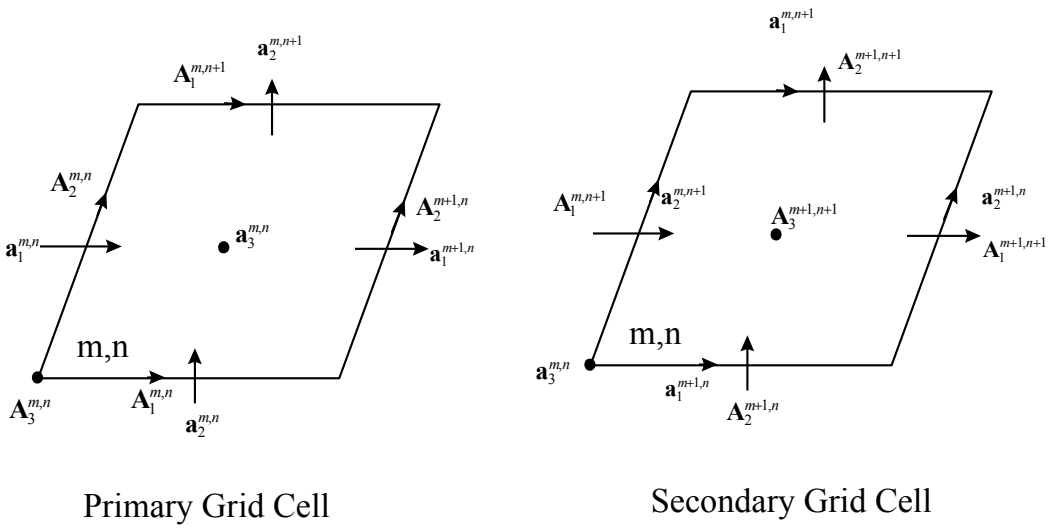

Figure 9 – Vector relations for a primary and secondary grid face.

$$V^3_{i,j,k_e} = \frac{\overrightarrow{A}^{\,e}_{3_{i,j,k}} \cdot \left(\left(\overrightarrow{A}^{\,h}_{1_{i,j,k}} + \overrightarrow{A}^{\,h}_{1_{i,j-1,k}} \right) \times \left(\overrightarrow{A}^{\,h}_{2_{i,j,k}} + \overrightarrow{A}^{\,h}_{2_{i-1,j,k}} \right) \right)}{4} \tag{72}$$

$$V^3_{i,j,k_h} = \frac{\overrightarrow{A}^{\,h}_{3_{i,j,k}} \cdot \left(\left(\overrightarrow{A}^{\,e}_{1_{i,j,k}} + \overrightarrow{A}^{\,e}_{1_{i,j+1,k}} \right) \times \left(\overrightarrow{A}^{\,e}_{2_{i,j,k}} + \overrightarrow{A}^{\,e}_{2_{i+1,j,k}} \right) \right)}{4}. \tag{73}$$

Here the computed contravariant field values are normalized by *length* and the covariant field values are scaled by *length*. Figure 9 illustrates the indexing structure for the dual grid for primary grid vectors $\overrightarrow{A}_i$ and secondary grid vectors $\overrightarrow{a}_i$. Note that all variables denoted by a superscript(subscript) of h pertain to secondary grid field quantities while those with an e pertain to the primary grid.

The contravariant field updates of (59) through (64) are executed in a time-marching manner with each field value on the right-hand-side known, albeit indirectly, from previous computations. For non-orthogonal grids, the contravariant vectors and the covariant vectors are not aligned. Therefore, these contravariant field values must be projected onto each covariant edge using the relation

$$f_i = \sum_{j=1}^{3} g_{i,j} f^j \tag{74}$$

to render the field values which are required on the right hand side of the field updates. For a regular grid each of the terms in (74) are unambiguously defined.

If an irregular grid is used the correct choice of the unitary vectors which define each $g_{i,j}$ is somewhat ambiguous. Both field and vectorial averaging must be applied to accomplish (74) . This leads to error as each component f^i which contributes to (74) is computed from a unique local coordinate system defined by the face through which the field component f^i passes .

There are several reasonable manners by which each $g_{i,j}$ may be constructed. In general these are defined by

$$g_{i,j} = \overrightarrow{A}_i \cdot \overrightarrow{A}_j \tag{75}$$

where the $\overrightarrow{A}_i$ is the vector along which the desired covariant field F_i is located and ideally $\overrightarrow{A}_j$ is one of the remaining two covariant vectors of the local coordinate system to which $\overrightarrow{A}_i$ belongs *and* it belongs to the

local coordinate system to which F^j belongs. Clearly the second vector can not be uniquely chosen for a staggered grid where no vector triple is collocated. The vector integrity of one of the two coordinate systems in an individual component projection may be respected, but not both.

The first approach investigated respects the vector integrity of local coordinate system of the face to which the field value F_i belongs. To accomplish this, the vectors $\overrightarrow{A}_{j=(i+1) \bmod 3}$, $\overrightarrow{A}_{j=(i+2) \bmod 3}$ are chosen from the local face through which F_i passes. Note that these vectors are defined by the *dual* grid from that of $\overrightarrow{A}_i$. These vectors are defined from the average value of each of the opposing sets of edges which define the face penetrated by edge i. The self term of the projection is defined by $\overrightarrow{A}_{j=i} = \overrightarrow{A}_i$. In this manner, a unique set of $g_{i,j}$ exist for each edge in both the secondary and primary grids. This projection method is referred to as G^{avg}.

The second approach favors the integrity of the coordinate system to which the projected field value F^j and corresponding unitary vector $\overrightarrow{A}_j$ belongs. For this method $\overrightarrow{A}_j$ is defined by the edge vector which is spatially aligned with F^j and in the *same* grid. This projection method requires a separate projection for each of the four components which contribute to F_i and thus is more computational expensive than the G^{avg} approach. This method is referred to as the G^4 approach.

A final technique recognizes that the vector length of the second term of the projections of G^{avg} could be inconsistent with that of the projected field F^j. To correct this, the projection technique of G^{avg} is applied with length normalization and scaling in an attempt to minimize error. Again four separate projections are required for this technique. This projection technique is referred to as G^{scaled} .

Mathematically, the projections G^{avg} and G^{scaled} require a projection of the form

$$f_i = g_{i,i} f^j + \sum_{j=i+1}^{(i+2) \bmod 3} \sum_{m=1}^{4} g_{i,j} f^j \tag{76}$$

where each field value for $i \neq j$ are one of the four averaged field components in (40) through (45).

A global stability criterion can not be formulated for this method due to the irregularness of the grid. A stability relation may be formulated on a cell by cell basis however using the curvilinear coordinate system composed of the unitary vectors of each face. Using a similar method as was described in the previous section, the stability is given as

$$\Delta_t \leq \frac{1}{c \sup \sqrt{\sum_{j=1}^{3} \sum_{i=1}^{3} |g^{i,j}|}} \tag{77}$$

where the sup operator denotes the maximum value throughout the entire space on both the primary and secondary grids.

A. NFDTD Results

The round wire transmission line is a challenging geometry for studying the effects of proper contour modeling[16]. This geometry is studied here with an irregular grid applied to the wire cross-section. The discretization is illustrated in Figure 10. In this illustration a PMC is placed at the center of the two wires to utilize even symmetry which exists, while a PEC plane is placed between the two wires to capitalize on the odd symmetry of this dimension. The geometry is 70 cells in the longitudinal direction with a discretization of $\Delta_{u_3} = 0.5\ mm$. The geometry is terminated with a 10 cell PML absorbing boundary at the $+u_1$, $+u_2$, and $\pm u_3$ extents. The convergence characteristics of the characteristic impedance are studied to determine the effectiveness of the NFDTD. It is noted that the grid is gradually transitioned to an orthogonal grid toward the outer extents of the grid. This allows for a more simplistic and accurate implementation of the absorbing boundary. Care should be taken to accomplish the tapering slowly as to prevent grid size relate discontinuities. As a good practice, one should attempt to keep all element sizes on the same order in each dimension. Large cell size changes can lead to local first order error. For each discretization chosen the distance to the side-wall absorbing boundaries is kept constant. The radius of each wire is $a = 0.25\ mm$ and the distance between the two wires is $d = 0.9\ mm$.

The results of this study are illustrated in Figures 11 through 13. It is clear from these illustrations that the projection method denoted as G^{avg} is slightly more accurate for this geometry than the other methods

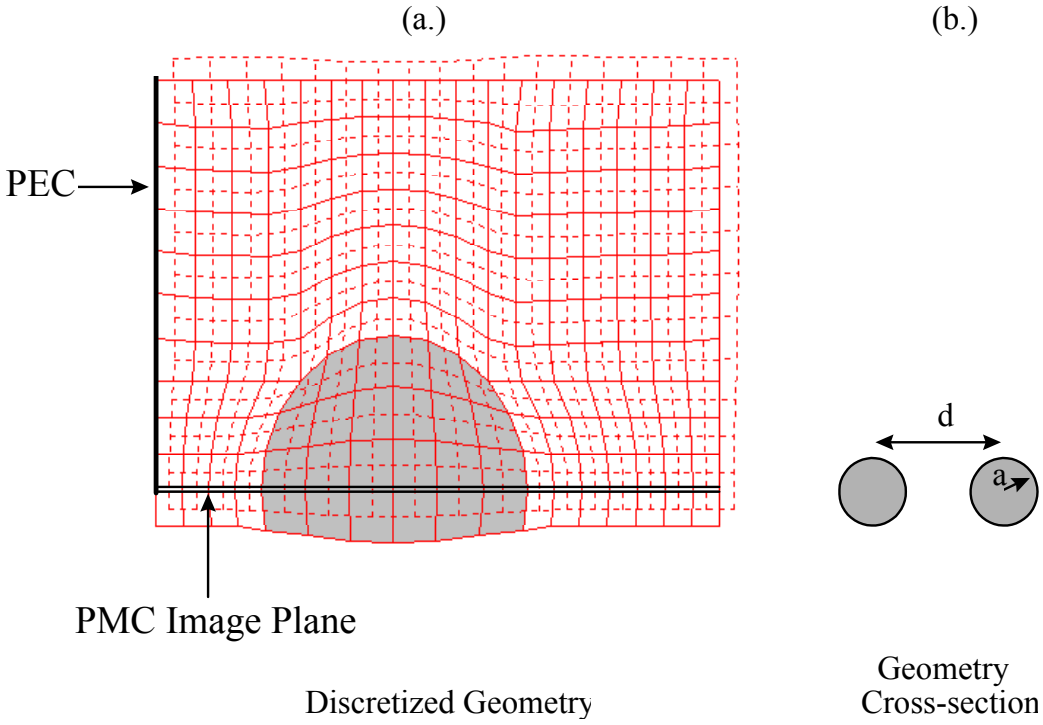

Figure 10 – Illustration of the discretization of one quadrant a round wire transmission line inluding secondary and primary grids. PEC and PMC planes are introduced to reflect odd and even symmetry about the x and y planes respectively.

implemented. For either of these projection methods, the results are much more accurate than is achievable using the orthogonal FDTD and as many as *forty* cells across the conductor.

V. Late-time Instability

It has been demonstrated by Gedney, Roden[17] that the stability relations given in 49, 77 are necessary yet not sufficient conditions for stability within non-orthogonal FDTD methods. For most problems, these constraints on the time step are sufficient such that over the period of time required to obtain necessary simulation data no instability is encountered. In the extreme late-time, however, instabilities can occur with *any* of the projection methods illustrated in this text as well as those which define the GenYee family of non-orthogonal methods.While the details will not be repeated here, the basic finding was that the update matrix formed by the curl operator combined with the projection operations must be symetric in order for the system to possess long term stability. In other words we must have that $G_{ij} = G_{ji}$. Since the G^4method accomplishes this symmetry, it is the most stable of all the projection methods demonstrated in this work. In addition to symmetry, the quality of the quality of the grid also impacts late-time stability. The grid characteristic which tends to cause instability is the degree of nonorthogonality present at each vertices. Specifically, if the angles between adjoining vectors are very small (less than 45 degrees) or very large (greater than 135 degrees) late-time stability can occur. As a result, the associated vectors are not sufficiently orthogonal to render an independent basis. For structured grids such as those in the NFDTD or GNFDTD methods, poor quality grids are very common. It has been found that a much more robust set of edge vectors may be generated using unstructured grids. Therefore, methods such as GenYee can render a more stable solution method. This issue is the subject of further research.

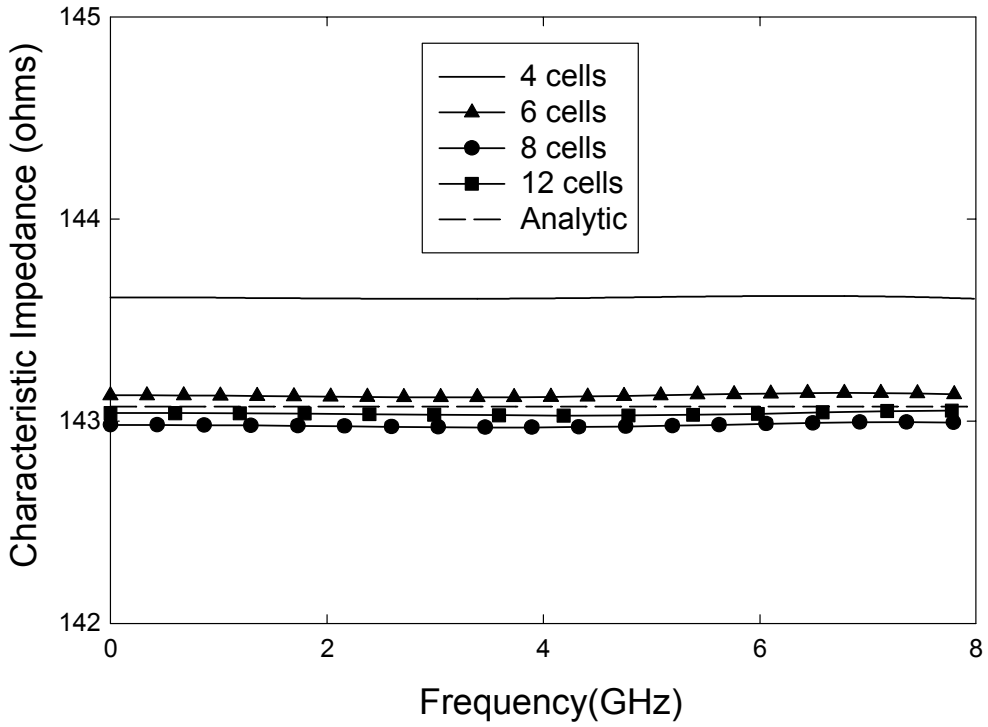

Figure 11 – Convergence of characteristic impedance of a round wire transmission line for the G^{avg} projection method.

VI. Conclusion

The non-orthogonal FDTD method provides a robust solution to full wave electromagnetic analysis in the presence of oblique or curved geometries. Two methods were examined for the analysis of complex geometries with curved boundaries. The GNFDTD method is applicable for geometries where curvature exists throughout the grid. It is accomplished by defining a global curvilinear coordinate system which conforms to the geometry and then solving Maxwell's equation in general curvilinear coordinates. The method can provide more accuracy than the orthogonal FDTD method as well as lower numerical dispersion. This method requires about three times the computations of the orthogonal FDTD method. For some problems, accurate gridding of a structure using the orthogonal FDTD technique may not be feasible and therefore the added computational burden of the GNFDTD method is acceptable.

The NFDTD is a more general approach to modeling irregular geometries. To accomplish this method, general curvilinear coordinate systems are introduced for each cell face in the grid and projections are constructed on a local basis. This method proved very robust in the analysis of round wire transmission lines. Late time instabilities were observed which could limit the application of this method for some highly resonant problems. It was found that a simple projection scheme using averaged projection values provided the most accurate solution. The most stable solution, however, was rendered by using a slightly less accurate approach which computed projections separately for each of the four fields projected. The additional cost of this projection method can certainly be justified for some problem sets.

References

[1] K. S. Yee, "Numerical Solution of Initial Boundary Value Problems Involving Maxwell's Equations in

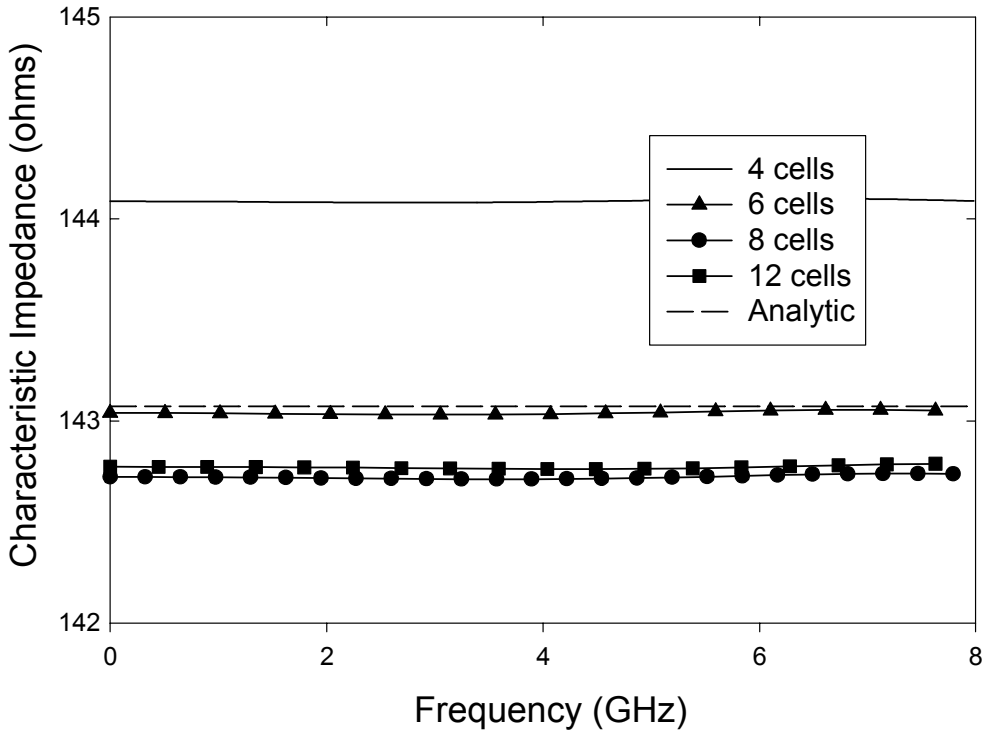

Figure 12 – Convergence of characteristic impedance of a round wire transmission line for the G^4 projection method.

Isotropic Media", *IEEE Trans. Antennas and Propagation,* vol. AP-14, no. 5, pp. 302-307, May 1966.

[2] J. A. Stratton, *Electromagnetic Theory,* New York, McGraw-Hill, 1941, pp. 38-47.

[3] R. Holland, "Finite-Difference Solution of Maxwell's Equations in Generalized Non-orthogonal Coordinates", *IEEE Trans. on Nuclear Science,* vol. NS-30, No. 6, December 1983.

[4] M. Fusco,"FDTD Algorithm in Curvilinear Coordinates", *IEEE Trans. on Antennas and Propagation,* vol. 38, no. 1,pp. 302-307, January 1990.

[5] J.-F. Lee, "Modeling Three-Dimensional Discontinuities in Waveguides Using Non-orthogonal FDTD Algorithm", *IEEE Transactions on Microwave Theory and Techniques*, vol. 40, no. 2, Feb. 1992.

[6] N. Madsen and R. Ziolkowski, "Divergence preserving discrete surface integral methods for Maxwell's equations using nonorthogonal unstructured grids", *Journal of Computational Physics,* vol. 119, no. 1, p. 34-35, January, 1995.

[7] S. D. Gedney and F. Lansing, "Full wave analysis of printed microstrip devices using a generalized-Yee algorythm",1993 IEEE Symposium on Antennas and Propagation Proceedings, Ann Arbor, MI, June 27-July 2, 1993.

[8] A. Taflove, *Computational Electrodynamics: The Finite Difference Time Domain Method*, Boston, Artech House, 1995.

[9] C. Railton, "Stabilised CPFDTD algorithm for the analysis of arbitrary 3D PEC structures", *IEE Proceedings - Microwaves, Antennas and Propagation*, vol.143, no.5, p. 367-72.

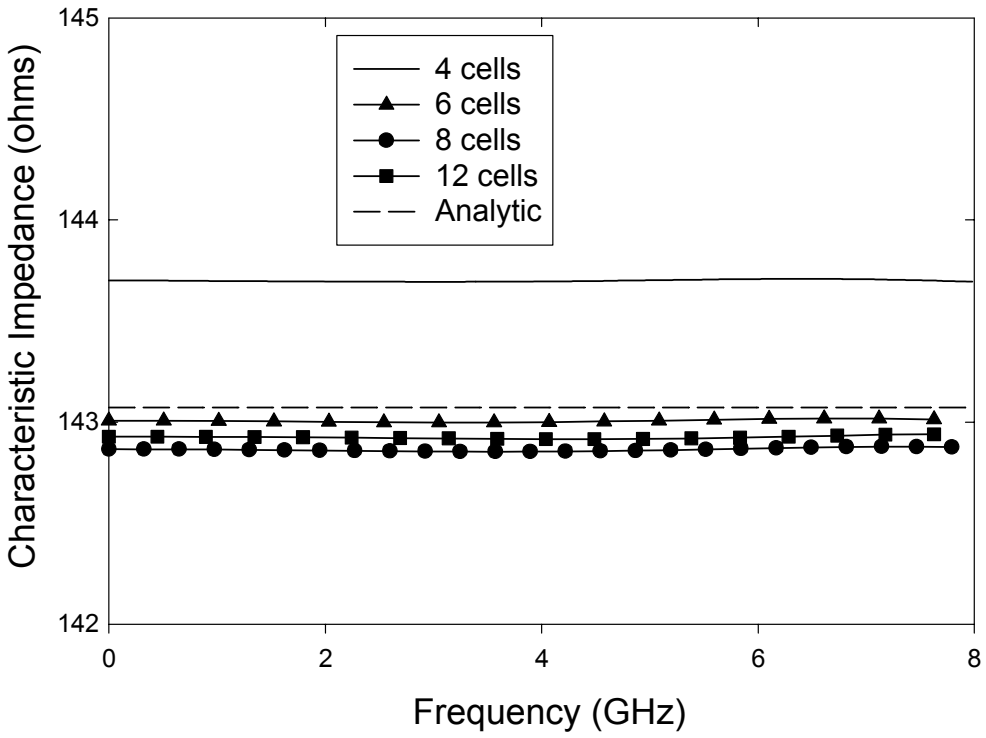

Figure 13 – Convergence of the characteristic impedance of a round wire transmission line using the G^{scale} projection method.

[10] Wenhua Yu, Raj Mittra, Accurate modelling of planar microwave circuits using conformal FDTD algorithm", Electronics Letters, March, 2000.

[11] Jiayuan Fang and Danwei Xeu, "Numerical Errors in the Computation of Impedances by FDTD Method and Ways to Eleminate Them", *IEEE Microwave and Guided Letters,* vol. 5.,No. 1 Jan. 1995.

[12] E.A. Navarro, C. Wu, P.Y. Chung and J. Litva, "Application of PML Superabsorbing Boundary Condition to Non-orthogonal FDTD Method", *Electronic Letters*, vol. 30, no.20,p. 1654-1656, 1994.

[13] J. W. Gibbs, *Vector Analysis*, Yale University Press, New Haven, Conn, 1941.

[14] S. Ramo, J. R. Whinnery, T. V. Duzer, *Fields and Waves in Communications Electronics,* Second Edition, p 252, John Wiley and Sons, New York. 1965.

[15] J. A. Roden, S. D. Gedney, "Efficient Implementation of the Uniaxial Based PML Media in Three-Dimensional Non-orthogonal Coordinates Using the FDTD Technique", in press *Microwave and Optical Tech. Let.* February 26, 1997.

[16] J. Alan Roden, *Broadband Electromagnetic Analysis of Complex Structures using the FDTD Technique in General Curvilinear Coordinates,* Ph.D. Dissertation, University of Kentucky, June, 1997.

[17] S.D. Gedney, J. A. Roden, "Numerical Stability of Nonorthogonal FDTD Methods", IEEE Trans. on Antennas and Propagation, vol 8, no 2, February, 2000.